DOI: 10.1002/ejic.200800958

The Magnetotransport Properties and a Neutron Diffraction Study of $Sr_{2-x}Nd_xFeMoO_6$ Double Perovskites

María Retuerto,*[a] María Jesús Martínez-Lope,[a] Mar García-Hernández,[a] and José Antonio Alonso[a]

Keywords: Perovskite phases / Colossal magnetoresistance / Neutron diffraction / Magnetic properties / Doping

New electron-doped derivatives of the Sr_2FeMoO_6 double perovskite have been studied. We report on the synthesis of the $Sr_{2-x}Nd_xFeMoO_6$ (x = 0, 0.2, 0.4 and 0.6) perovskite series by a wet chemistry procedure and its characterization. The evolution of the crystal and magnetic structure has been analyzed from neutron powder diffraction data. The partial replacement of Sr^{2+} cations by higher valence Nd^{3+} cations induces an injection of electrons into the Fe/Mo sublattice. A bond-valence study demonstrates that this electron-injection preferentially affects the Mo orbitals. This substitution leads to a distortion of the structure from tetragonal ($I4/m$) to monoclinic ($P2_1/n$) at room temperature for $x \geq 0.4$ and an increase of the disorder between Fe and Mo cations. This effect has severe consequences for the magnetic properties, notably a reduction of the saturation magnetization and a non-monotonic behavior of the Curie temperature. Magnetotransport measurements show a significant increment of the magnetoresistance at low temperature for high values of x.

Introduction

Interest in the family of double perovskites A_2FeMoO_6 (A = Ca, Sr, Ba) has been renewed recently due to their room temperature magnetoresistance properties.[1,2] Sr_2FeMoO_6 is understood to be a half metallic material with a completely polarized conduction band,[1] therefore its electronic transport properties can be influenced by the application of an external magnetic field.[3,4] The structure of A_2FeMoO_6 perovskites can be viewed as a regular arrangement of corner-sharing FeO_6 and MoO_6 octahedra alternating along the three directions of the crystal, with the large A cations occupying the voids in between the octahedra. Depending on the ionic radii of the A cation, the structure can be cubic (A = Ba), tetragonal (A = Sr) or monoclinic (A = Ca).[5,6]

The ferrimagnetic structure of the ideal Sr_2FeMoO_6 contains an ordered array of Fe^{3+} $3d^5$ (S = 5/2) spins antiferromagnetically coupled with Mo^{5+} $4d^1$ (S = 1/2) spins. In this model, the ideal saturation magnetization (M_s) would be 4 μ_B per formula unit. However, the actual value of M_s is always lower due to so-called anti-site disorder. Anti-site B-cation disorder (ASD) is defined as some Mo^{5+} cations occupying the position of the Fe^{3+} cations and vice versa. In regions of the crystal where anti-site defects occur, the Fe–O–Fe configuration gives rise to antiferromagnetic interactions[7–9] which decrease the saturation magnetization.

Sr_2FeMoO_6 has been widely studied due to its high Curie temperature (T_c) of around 415 K. It is believed that the ferrimagnetic Fe–O–Mo–O–Fe interaction is mediated by the itinerant down spin electrons of the Mo ions, thus it has been proposed[10] that an increase in the number of carriers in the spin-polarized conduction band would induce an enhancement of T_c. This injection of carriers could be attained by electron doping in the Fe/Mo sublattice arising from the substitution of Sr^{2+} by trivalent cations from the A sublattice. Previous studies on La-doped materials[11,12] have shown, however, that electron doping tends to reduce the charge difference between Fe and Mo cations, thereby promoting an increase in the ASD. This ASD produces unwanted effects in the magnetic and magnetotransport properties of the samples. Moreover, as ASD differs from sample to sample, pure electronic effects are masked, as has been shown in the La-substituted series.[11,12] Herein we report on our efforts to reduce the unwanted effects of ASD by doping with a smaller rare-earth cation, namely Nd^{3+}, in order to isolate the effect of carrier doping in the conduction band. Furthermore, we attempted to reduce the ASD by using a wet chemistry procedure that yields a homogeneous cationic distribution at atomic levels, as demonstrated for the undoped Sr_2FeMoO_6 perovskite.[13] Azad et al. have reported[14] the structural and magnetic properties of the Nd-doped series up to x = 0.4. The present study extends this series up to x = 0.6 and describes a non-monotonic behaviour of T_c. Furthermore, we include the magnetotransport properties of the doped oxides, which exhibit an unexpected increase in the magnetoresistance (MR) for high doping levels.

[a] Instituto de Ciencia de Materiales de Madrid, CSIC, Cantoblanco, 28049 Madrid, Spain

Results and Discussion

Crystallographic Structures

$Sr_{2-x}Nd_xFeMoO_6$ oxides were obtained as black well-crystallized powders. The XRD patterns at room temperature are characteristic of a perovskite structure (Figure 1) and show superstructure reflections corresponding to long-range Fe/Mo ordering [e.g., (011) and (013)]. The intensity of the superstructure reflections decreases as x increases due to an increment of the ASD level (inset Figure 1). The ASD values were determined by Rietveld analysis of the XRD data.

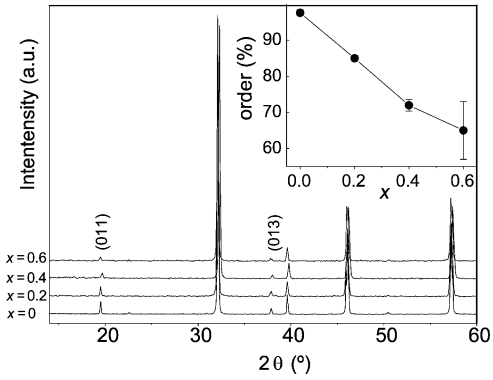

Figure 1. XRD patterns (Cu-K_α) for the $Sr_{2-x}Nd_xFeMoO_6$ series (x = 0, 0.2, 0.4, 0.6) showing the first two superstructure peaks related to Fe/Mo ordering. The inset shows the variation of the Fe/Mo ordering along the series.

The crystal structure refinement was performed from high-resolution neutron powder diffraction (NPD) data collected at room temperature and 10 K with a wavelength of 1.594 Å. In a first attempt, the crystal structure was defined considering the tetragonal model *I*4/*m*. This model corresponds to an ordered double perovskite with two crystallographically independent B positions (Fe and Mo) and two kinds of nonequivalent oxygen atoms (O1 and O2). This model gives a reasonable fit for $x < 0.4$ at room temperature and $x < 0.2$ at low temperature. However, for $x \geq 0.4$ at room temperature (and $x \geq 0.2$ at 10 K) the splitting of some reflections at high diffraction angles made it necessary to consider a lowering in the crystal symmetry with respect to the tetragonal model. The structure was successfully refined in the monoclinic $P2_1/n$ space group, which contains two different positions for Fe and Mo and three kinds of nonequivalent oxygen atoms (O1, O2 and O3), all in general (x,y,z) positions. Figure 2 illustrates this feature for x = 0.2 at 10 K; the tetragonal model (Figure 2, a) is not able to explain all the Bragg reflections, whereas the monoclinic space group (Figure 2, b) accounts for all the peak intensities. This reduction in symmetry is very subtle and, indeed, was overlooked in a previous publication.[14]

In all cases, the monoclinic beta angle is very close to 90°, thus indicating a strong pseudo-orthorhombic character of the unit cell. This symmetry and space group are known to be adopted by other related and well-known double perovskites as Nd_2MgTiO_6,[15] Ca_2CaUO_6[16] and

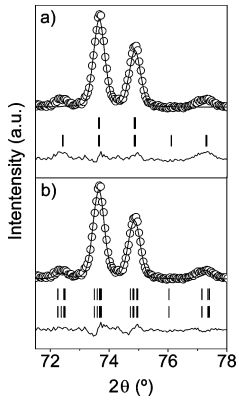

Figure 2. Observed (circles), calculated (full line) and difference (bottom) NPD Rietveld profiles of $Sr_{1.8}Nd_{0.2}FeMoO_6$ at 10 K. The two sets of vertical lines correspond to the crystallographic and magnetic structures. The upper and lower figures correspond to refinements in the *I*4/*m* and $P2_1/n$ space groups, respectively.

Ca_2FeMoO_6,[17] with small tolerance factors. The observed reduction in symmetry of the adopted space group is mainly due to subtle tilts of the BO_6 octahedra, which result in small shifts of the oxygen positions and which can be detected by neutron diffraction. Figure 3 illustrates the quality of the agreement between the full observed and calculated NPD profiles at room temperature for x = 0.4 ($P2_1/n$).

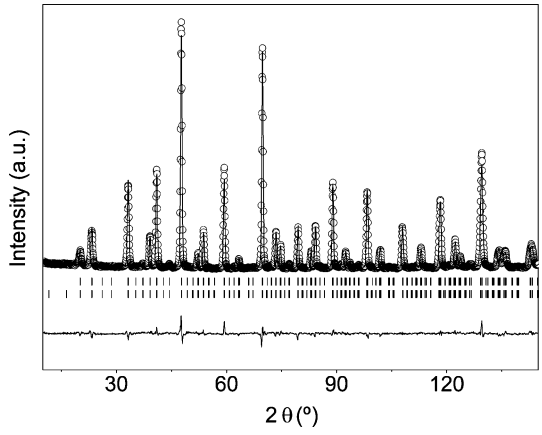

Figure 3. Rietveld fit from NPD data for $Sr_{1.6}Nd_{0.4}FeMoO_6$ oxide. Observed (circles), calculated (full line) and difference (bottom) profiles at room temp. The second series of Bragg positions correspond to the magnetic structure.

The variation of the unit-cell parameters at room temperature and 10 K is shown in Figure 4. The cell volume (Figure 4, b) exhibits a very slight variation at high doping levels due to a competition between the introduction of a smaller cation in the Sr sublattice [the radius of Nd^{3+} (1.27 Å) is smaller than that of Sr^{2+} (1.44 Å)] and the effective injection of electrons, which tends to expand the lattice volume.

The structural parameters at room temperature and 10 K are listed in Tables 1 and 2. Table 3 contains the main interatomic distances and angles across the series. Figure 5 (a) displays the evolution of the average Fe–O and Mo–O bond lengths with Nd content. Thus, whereas the Fe–O distances diminish slightly along the series, the Mo–O distances in-

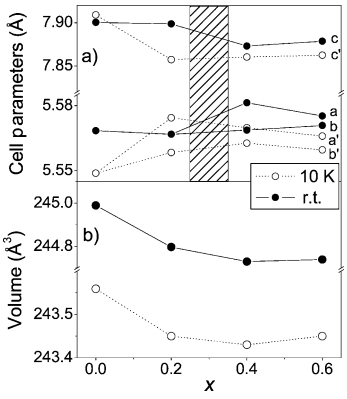

Figure 4. Evolution of (a) the unit-cell parameters and (b) the volume in the $Sr_{2-x}Nd_xFeMoO_6$ series (x = 0, 0.2, 0.4, 0.6).

crease smoothly with Nd content. The variation of the superexchange Fe–O–Mo angles along the series, shown in part b of Figure 5, clearly indicates an increase of the tilting angle with x. This effect corresponds to the expected reduction of the tolerance factor due to the introduction of the smaller Nd^{3+} cations and the expansion of the BO_6 octahedra as a consequence of the electron injection.

As we are especially interested in investigating the microscopic effects of electron-doping on the different cations at the B-sublattice of the perovskite, we applied Brown's phenomenological Bond-Valence Model (BVS),[18] which gives us an estimation of the actual valences on the cations and anions of a given structure by means of an empirical relationship between the observed bond lengths and the valence of a bond, to this system. The valences along the series,

Table 1. Atomic parameters and agreement factors after the Rietveld refinement of NPD patterns for the $Sr_{2-x}Nd_xFeMoO_6$ series at room temp.

	x = 0	x = 0.2		x = 0.4	x = 0.6
*I*4/*m*			*P*2$_1$/*n*		
a [Å]	5.56863(5)	5.56689(9)	*a* [Å]	5.5823(2)	5.5782(3)
b [Å]	5.56863(5)	5.56685(8)	*b* [Å]	5.5689(1)	5.5711(2)
c [Å]	7.9007(1)	7.8991(2)	*c* [Å]	7.8727(2)	7.8753(3)
			β [°]	89.987(1)	89.997(1)
V [Å^3]	244.999(4)	244.796(8)	*V* [Å^3]	244.74(1)	244.74(2)
Sr/Nd 4d(0 1/2 1/4)			Sr/Nd 4e(*x y z*)		
			x	0.99995(8)	0.9994(1)
			y	0.00651(8)	0.0101(1)
			z	0.2506(3)	0.2497(4)
B [Å^2]	0.94(2)	1.08(2)	*B* [Å^2]	1.15(2)	1.21(3)
Fe 2a(0 0 0)			Fe 2b(1/2 0 1/2)		
B [Å^2]	0.6(1)	0.45(6)	*B* [Å^2]	1.2(1)	0.66(5)
Mag. mom. [μ_B]	2.0(1)	1.6(3)	Mag. mom. [μ_B]	1.2(2)	1.5(4)
Occupancy[a]			Occupancy		
Fe(2a)	0.970(8)	0.854(8)	Fe(2b)	0.72(2)	0.65(8)
Mo(2a)	0.030(8)	0.146(8)	Mo(2b)	0.28(2)	0.35(8)
Mo 2b(0 0 1/2)			Mo 2d(1/2 0 0)		
B [Å^2]	0.4(1)	0.905(9)	*B* [Å^2]	–0.3(1)	0.2(5)
Mag. mom. [μ_B]	–0.9(1)	–1.0(3)	Mag. mom. [μ_B]	–1.5(2)	–1.5(4)
Occupancy[a]			Occupancy		
Mo(2b)	0.970(8)	0.854(8)	Fe(2d)	0.72(2)	0.65(8)
Fe(2b)	0.030(8)	0.146(8)	Mo(2d)	0.28(2)	0.35(8)
O1 4e(0 0 *z*)			O1 4e(*x y z*)		
			x	0.04552(6)	0.0526(1)
			y	0.5008(1)	0.5000(1)
z	0.254(1)	0.2518(1)	*z*	0.2500(3)	0.2507(6)
B [Å^2]	0.92(4)	1.32(6)	*B* [Å^2]	1.20(6)	1.20(9)
O2 8 h(*x y* 0)			O2 4e(*x y z*)		
x	0.2727(8)	0.27688(9)	*x*	0.7400(1)	0.7363(3)
y	0.2336(6)	0.22291(9)	*y*	0.2634(2)	0.2665(3)
			z	0.02237(8)	0.02301(9)
B [Å^2]	1.09(3)	1.39(4)	*B* [Å^2]	1.1(1)	1.1(1)
			O3 4e(*x y z*)		
			x	0.2253(1)	0.2230(3)
			y	0.2274(2)	0.2213(3)
			z	0.97091(8)	0.9673(1)
			B [Å^2]	1.3(1)	1.2(2)
Reliability factors					
χ^2	2.64	5.85	χ^2	3.91	3.82
R_p [%]	3.78	4.99	R_p [%]	3.94	4.38
R_{wp} [%]	4.71	6.46	R_{wp} [%]	4.94	5.40
R_I [%]	2.90	2.67	R_I [%]	2.50	2.76
$R_{mag.}$ [%]	9.31	10.9	$R_{mag.}$ [%]	9.79	11.8

[a] The Fe/Mo occupancy factors were determined from XRD data and fixed during refinement of the NPD data.

Table 2. Atomic parameters and agreement factors after the Rietveld refinement of NPD patterns for the $Sr_{2-x}Nd_xFeMoO_6$ series at 10 K.

	$x = 0$		$x = 0.2$	$x = 0.4$	$x = 0.6$
*I*4/*m*		*P*2$_1$/*n*			
a [Å]	5.54914(6)	*a* [Å]	5.5746(1)	5.5706(2)	5.5671(3)
b [Å]	5.54914(6)	*b* [Å]	5.5586(1)	5.5600(2)	5.5626(2)
c [Å]	7.90955(9)	*c* [Å]	7.8576(2)	7.8603(3)	7.8615(3)
		β [°]	89.998(6)	89.992(1)	89.999(7)
V [Å^3]	243.559(5)	*V* [Å^3]	243.482(9)	243.45(1)	243.45(2)
Sr/Nd 4d(0 1/2 1/4)		Sr/Nd 4e(*x y z*)			
		x	0.99891(7)	0.9987(1)	0.9981(1)
		y	0.0042(1)	0.00911(7)	0.01139(9)
		z	0.2507(2)	0.2500(3)	0.2493(4)
B [Å^2]	0.44(2)	*B* [Å^2]	0.66(2)	0.80(3)	0.92(4)
Fe 2a(0 0 0)		Fe 2b(1/2 0 1/2)			
B [Å^2]	0.58(6)	*B* [Å^2]	0.94(9)	1.2(1)	0.68(3)
Magnetic moment [μ_B]	3.60(7)	Magnetic moment [μ_B]	3.23(8)	2.9(1)	2.5(2)
Mo 2b(0 0 1/2)		Mo 2d(1/2 0 0)			
B [Å^2]	0.04(7)	*B* [Å^2]	–0.3(2)	–0.5(1)	0.02(3)
Mag. mom. [μ_B]	–0.42(6)	Magnetic moment [μ_B]	–0.66(7)	–1.02(9)	–1.5(2)
O1 4e(0 0 *z*)		O1 4e(*x y z*)			
		x	0.04358(5)	0.05149(7)	0.0566(1)
		y	0.5000(1)	0.4989(1)	0.4975(1)
z	0.2580(5)	*z*	0.2498(3)	0.2501(3)	0.2505(7)
B [Å^2]	0.51(3)	*B* [Å^2]	0.82(6)	0.89(7)	1.05(9)
O2 8 h(*x y* 0)		O2 4e(*x y z*)			
x	0.2816(5)	*x*	0.7450(1)	0.7377(2)	0.7342(3)
y	0.2271(5)	*y*	0.2606(2)	0.2659(2)	0.2688(3)
		z	0.0213(1)	0.02408(1)	0.02505(9)
B [Å^2]	0.61(2)	*B* [Å^2]	0.9(2)	0.9(1)	0.8(1)
		O3 4e(*x y z*)			
		x	0.2281(1)	0.2227(2)	0.2212(3)
		y	0.2338(2)	0.2248(2)	0.2198(3)
		z	0.9755(1)	0.9710(1)	0.9660(1)
		B [Å^2]	0.8(2)	1.0(2)	1.0(2)
Reliability factors					
χ^2	4.11	χ^2	4.203	3.81	4.14
R_p [%]	4.51	R_p [%]	4.54	4.71	4.73
R_{wp} [%]	5.63	R_{wp} [%]	5.65	5.91	5.82
R_I [%]	2.78	R_I [%]	2.82	3.03	2.86
$R_{mag.}$ [%]	4.04	$R_{mag.}$ [%]	4.09	3.11	5.05

Table 3. Main interatomic distances [Å] and angles [°] for the $Sr_{2-x}Nd_xFeMoO_6$ series at room temp. and 10 K.

	*I*4/*m*			*P*2$_1$/*n*				
	$x = 0$		$x = 0.2$		$x = 0.4$		$x = 0.6$	
	room temp.	10 K	room temp.	10 K	room temp.	10 K	room temp.	10 K
FeO_6 octahedra								
Fe–O1 (×2)	2.008(8)	2.041(4)	1.989(1)	1.981(2)	1.984(2)	1.985(3)	1.996(5)	1.994(5)
Fe–O2 (×2)	1.999(4)	2.007(3)	1.9788(6)	1.998(1)	1.995(1)	1.994(1)	1.972(1)	1.970(2)
Fe–O3 (×2)				2.0059(9)	2.0021(9)	2.000(1)	2.006(2)	2.004(2)
Fe–O	2.002(4)	2.018(3)	1.9823(3)	1.9949(6)	1.9934(6)	1.9929(8)	1.991(1)	1.990(1)
MoO_6 octahedra								
Mo–O1 (×2)	1.942(8)	1.914(4)	1.960(1)	1.978(2)	1.985(2)	1.987(3)	1.985(5)	1.987(5)
Mo–O2 (×2)	1.950(4)	1.940(3)	1.9804(6)	1.954(1)	1.9680(9)	1.966(1)	1.994(2)	1.994(2)
Mo–O3 (×2)				1.960(1)	1.985(1)	1.983(1)	1.993(2)	1.994(2)
Mo–O	1.946(4)	1.931(3)	1.9738(3)	1.9642(6)	1.9793(6)	1.9787(8)	1.991(1)	1.991(1)
Angles around O								
Fe–O1–Mo	180.0	180.0	180.0	165.9(1)	165.3(1)	163.4(1)	163.0(2)	161.8(2)
Fe–O2–Mo	171.0(2)	167.5(1)	167.68(2)	169.62(4)	168.49(4)	167.27(4)	167.44(7)	166.12(7)
Fe–O3–Mo				165.87(4)	162.95(4)	162.23(4)	160.50(7)	159.61(7)
Fe–O–Mo	174(2)	171.7(1)	171.78(2)	167.13(4)	165.58(4)	164.30(4)	163.64(7)	162.34(7)
Bond valence Fe	2.839(7)	2.91(2)	3.067(3)	2.964(6)	2.976(7)	2.980(8)	2.99(1)	3.00(1)
Bond valence Mo	5.496(9)	5.37(3)	5.009(6)	5.14(1)	4.93(1)	4.94(1)	4.78(2)	4.78(2)

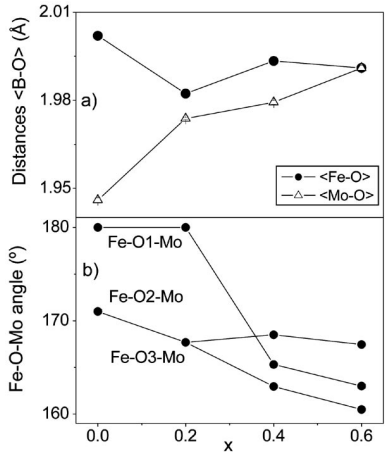

Figure 5. (a) Evolution of the Fe–O and Mo–O bond lengths with x. (b) Nd-doping dependence of the Fe–O–Mo bond angles at room temp.

calculated from the room temperature data using this approach, are represented in Figure 6 (a). It is interesting to note that the valence for Mo cations decreases as x increases, whereas the Fe valence remains almost constant across the series (Table 3). The difference between the radii of the Fe^{2+} (0.78 Å) and Fe^{3+} (0.654 Å) cations is bigger than that between the radii of the various Mo ions [$r(Mo^{4+})$ = 0.65, $r(Mo^{5+})$ = 0.61 and $r(Mo^{6+})$ = 0.59 Å]. It is worth mentioning that the metal–oxygen distances, and hence the oxidation states, are influenced by the fact that we are dealing with mixed occupation at the metal sites. In other words, the M–O distances obtained from the refinements are weighted by Fe and Mo fractions at nominally "Fe" and "Mo" sites. We have to work with these site-averaged distances since it is not possible to obtain the absolute Fe–O (Mo–O) values from diffraction data. Furthermore, they are affected by a rather large error, especially at high levels of anti-site disorder. By taking different ordering coefficients with known Fe–O/Mo–O distances, we have estimated the error inherent in dealing with site-averaged distances. At the highest level of ASD exhibited in our series (x = 0.6 sample), the deviation in the metal–oxygen distance (0.3%) and the calculated oxidation state (0.4%) fall well within the experimental error. In other words, the tendencies shown in Figure 6 (a) must be attributed to electronic effects.

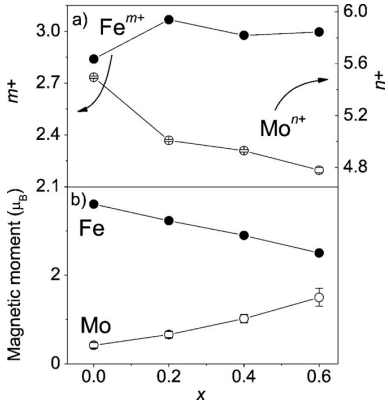

Figure 6. (a) Evolution of Fe^{m+} and Mo^{n+} oxidation states with electron doping in the series $Sr_{2-x}Nd_xFeMoO_6$ as obtained from Brown's bond valence model at room temp. (b) Evolution of the magnetic moments obtained from the NPD magnetic refinement at 10 K.

Magnetic Structures

Refinement of the low-temperature (10 K) magnetic structures allowed us to determine the ordered magnetic moments on the Fe and Mo sites. Table 2 and part b of Figure 6 show that the Mo magnetic moments increase significantly (in absolute terms) along the series. This increase could be due to the injection of electrons into the Mo band or an increase in the number of Fe ions in Mo positions upon Nd doping. The magnetic moment in the Fe position decreases because the Mo ions in this position increase with x. Not all the electrons are introduced into this position, however, as the magnetic moment decreases.

Magnetic Measurements

A plot of the magnetic susceptibility vs. temperature for the different members of the $Sr_{2-x}Nd_xFeMoO_6$ series is shown in Figure 7. The susceptibility above T_c drops to suitably small values, thereby indicating the absence of magnetic impurities like Fe metal. The T_c values were evaluated from the derivatives of the susceptibility curves. As shown in the inset, the Curie temperature diminishes at the beginning of the series since the increment of the structural distortion (bending of the superexchange Fe–O–Mo angles) prevails over the electronic effect. For high doping levels, T_c increases because the electron injection is able to overcome the structural distortion, which leads to an improvement of the long-range magnetic interactions. It is worth noting that we observe a distinct evolution of T_c with respect to that described previously,[14] where the authors reported a monotonic increase of T_c with the Nd doping level. Our observation of an initial decrease of T_c and then an increase for

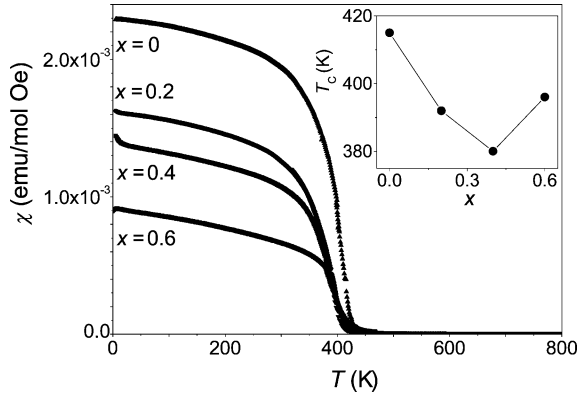

Figure 7. Susceptibility at 1000 Oe for $Sr_{2-x}Nd_xFeMoO_6$ oxides (x = 0, 0.2, 0.4, 0.6). The inset shows the variation of T_c along the series, as calculated from the first derivative of the $M(T)$ curve.

x = 0.6 is due to the better quality of our x = 0 sample, which displays a higher M_s and T_c and means that the x = 0.2 and 0.4 samples exhibit a decrease of both values due to an increase in the anti-site disordering, which for x = 0.6 is overcome by the electron-injection effect.

A plot of magnetization vs. magnetic field at 5 K (Figure 8) shows the hysteresis curves of the series. An almost complete saturation of the magnetic moment is reached in all the samples. The saturation magnetization decreases with doping (inset of Figure 8) due to an increased disorder and consequent enhancement of the Fe–O–Fe antiferromagnetic clusters.

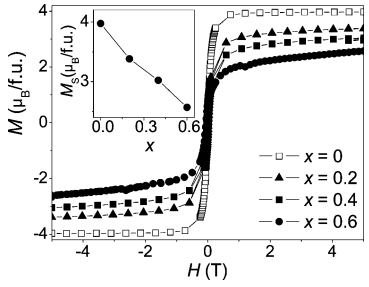

Figure 8. Magnetization vs. field isotherms (T = 5 K) for the $Sr_{2-x}Nd_xFeMoO_6$ series (x = 0, 0.2, 0.4, 0.6).

Magnetotransport Measurements

The magnetotransport properties at 300 and 5 K are illustrated in Figure 9. Two different regions can clearly be distinguished in the MR isotherms: the magnetoresistance in the low-field region (LFMR) originates from the spin scattering process across the grain boundaries, whilst in the high-field region (HFMR) it is mainly intrinsic in origin. At room temperature, the MR decreases monotonically with doping. The LFMR is mostly determined by the level of ASD, thus accounting for the huge decrease in LFMR from that observed in the pure sample. The slope of the HFMR remains almost constant because this region is less dependent on the disorder. It is worth highlighting that, at 5 K, LFMR increases steadily (inset of Figure 9, b) for $x \geq 0.2$, eventually overcoming the value of the pure compound for x = 0.6. We suggest that this abnormal behaviour could be due to the introduction of a magnetic rare earth atom which, at very low temperature, may be polarized by the molecular field of Fe spins, thus enhancing the spin scattering mechanism upon application of an external field and reinforcing the MR effect.

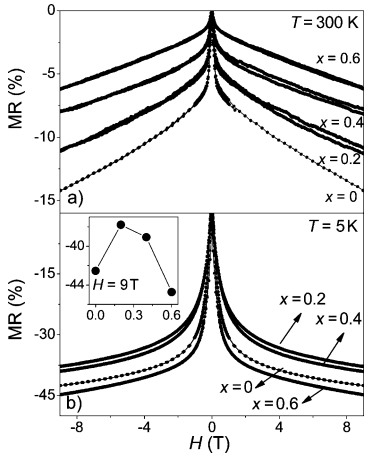

Figure 9. MR vs. magnetic field isotherms at 300 and 5 K for the $Sr_{2-x}Nd_xFeMoO_6$ series (x = 0, 0.2, 0.4, 0.6). MR(H) = $100 \times \{[R(H) - R(0)]/R(0)\}$.

Conclusions

In conclusion, we have studied the structural, magnetic and magnetotransport properties of the $Sr_{2-x}Nd_xFeMoO_6$ series up to x = 0.6. The Sr^{2+} cations are partially replaced by smaller Nd^{3+} cations, which produces a distortion of the structure from a tetragonal to a monoclinic symmetry at high doping levels as well as a structural transition of the sample with x = 0.2 at low temperatures. The unit-cell volume exhibits a slight variation at high Nd doping levels due to a competition between steric effects and the effective injection of electrons. The valence of the Mo cations decreases as x increases, whereas the Fe valence remains almost constant across the series, thus indicating that the electron injection preferentially affects the Mo cations. The disorder between Fe and Mo increases along the series and the ASD promotes the appearance of antiferromagnetic clusters that affect the ferromagnetic interaction, thereby decreasing the saturation magnetization. However, for high doping levels, the electron injection is able to overcome the structural distortion, which leads to an improvement of the long-range magnetic interactions and an increase of T_c. The magnetotransport properties of the series indicate a magnetoresistive behaviour for all members of the series, with MR values of around –40% at 5 K for H = 9 T. The abnormal increase of MR for x = 0.6, which reaches a value higher than that of the x = 0 compound, is interesting; this could be an effect of the introduction of a magnetic rare earth atom into the system.

Experimental Section

$Sr_{2-x}Nd_xFeMoO_6$ (x = 0, 0.2, 0.4, 0.6) compounds were prepared in polycrystalline form by a soft-chemistry procedure designed to obtain very reactive precursors. Thus, stoichiometric amounts of $Sr(NO_3)_2$, $FeC_2O_4{\cdot}2H_2O$, $(NH_4)_6Mo_7O_{24}{\cdot}4H_2O$ and Nd_2O_3 were dissolved in citric acid and a small amount of nitric acid (to dissolve the $FeC_2O_4{\cdot}2H_2O$ and Nd_2O_3). The citrate and nitrate solutions were slowly evaporated to give organic resins containing a homogeneous distribution of the involved cations. These resins were dried at 120 °C and then decomposed at 600 °C. The organic materials and nitrates were eliminated by a subsequent treatment at 800 °C in air. This treatment gave rise to homogeneous precursor materials. For the Nd-doped samples with $x < 0.4$, the precursors were treated at 1200 °C for 12 h in an H_2/Ar (1%/99%) reducing flow. For Nd-doped samples with $x \geq 0.4$, reduction of the precursors in an H_2/N_2 (5%/95%) flow at 850 °C proved necessary before the final synthesis at 1200 °C in an H_2/Ar (1%/99%) reducing flow.

The samples were characterized by X-ray diffraction (XRD) using a Bruker-AXS D8 diffractometer (40 kV, 30 mA), controlled by the DIFFRACT^{plus} software, in Bragg–Brentano reflection geometry with Cu-K_α radiation (λ = 1.5418 Å). A secondary graphite monochromator allowed the complete removal of Cu-K_β radiation. The data were recorded between 10 and 100° 2θ in steps of 0.05°. The slit system was selected to ensure that the X-ray beam was completely within the sample at all 2θ angles.

Neutron powder diffraction (NPD) experiments were carried out in the high-resolution powder diffractometer D2B (λ = 1.594 Å) at the ILL, Grenoble. All the patterns were collected at room temperature and 10 K in a displex unit. Refinement of the crystal and magnetic structures was performed by the Rietveld method, using the FULLPROF refinement program.[19] A pseudo-Voigt function was chosen to generate the line shape of the diffraction peaks. The following parameters were refined in the final run: scale factor, background coefficients, zero-point error, pseudo-Voigt corrected for asymmetry parameters, positional coordinates, isotropic thermal factors and occupancy factors for oxygen atoms. The coherent scattering lengths for Sr, Nd, Fe, Mo and O were 7.02, 7.69, 3.635, 6.720 and 5.803 fm, respectively.

The magnetic measurements were performed with a commercial superconducting quantum interference device magnetometer (SQUID). The susceptibility was measured in a 0.1-T magnetic field in the temperature range 5–800 K. An isothermal magnetization curve was obtained for magnetic fields of between –5 and 5 T at a temperature of 5 K.

Acknowledgments

We acknowledge financial support from the Spanish Ministerio de Educación y Ciencia (MEC) for the projects MAT2007-60536 and MAT2005-06024-C02-01 and are grateful to Institut Laue-Langevin (ILL) for use of their facilities.

[1] K. I. Kobayashi, T. Kimura, H. Sawada, K. Terakura, Y. Tokura, *Nature* **1998**, *395*, 677.
[2] T. H. Kim, M. Uehara, S.-W. Cheong, S. Lee, *Appl. Phys. Lett.* **1999**, *74*, 1737.
[3] Y. Tomioka, T. Okuda, Y. Okimoto, R. Kumain, K. I. Kobayashi, *Phys. Rev. B* **2000**, *61*, 422.
[4] Z. Fang, K. Terakura, J. Kanamori, *Phys. Rev. B* **2001**, *63*, 180407.
[5] R. P. Borges, R. M. Thomas, C. Cullinan, J. M. D. Coey, R. Suryanarayanan, L. Ben-Dor, L. Pinsard-Gaudart, A. Revcolevschi, *J. Phys: Condens. Matter* **1999**, *11*, L445.
[6] C. Ritter, M. R. Ibarra, L. Morellón, J. Blasco, J. García, J. M. De Teresa, *J. Phys: Condens. Matter* **2000**, *12*, 8295.
[7] D. Sanchez, J. A. Alonso, M. García-Hernández, M. J. Martinez-Lope, J. L. Martínez, A. Mellergard, *Phys. Rev. B* **2002**, *65*, 104426.
[8] L. Balcells, J. Navarro, M. Bibes, A. Roig, B. Martínez, J. Fontcuberta, *Appl. Phys. Lett.* **2001**, *78*, 781.
[9] H. Yanagihara, M. B. Salamon, Y. Lyanda-Geller, Sh. Xu, Y. Moritomo, *Phys. Rev. B* **2001**, *64*, 214407.
[10] D. D. Sarma, P. Mahadevan, T. Saha-Dasgupta, R. Sugata, K. Ashwani, *Phys. Rev. Lett.* **2000**, *85*, 2549.
[11] D. Serrate, J. M. De Teresa, J. Blasco, M. R. Ibarra, L. Morellón, C. Ritter, *Appl. Phys. Lett.* **2002**, *80*, 4573.
[12] D. Sánchez, J. A. Alonso, M. García-Hernández, M. J. Martínez-Lope, M. T. Casais, J. L. Martinez, *J. Mater. Chem.* **2003**, *13*, 1771.
[13] M. Retuerto, J. A. Alonso, M. J. Martinez-Lope, J. L. Martinez, M. García-Hernández, *Appl. Phys. Lett.* **2004**, *85*, 266.
[14] A. K. Azad, S.-G. Eriksson, A. Khan, A. Eriksson, M. Tseggai, *J. Solid State Chem.* **2006**, *179*, 1303.
[15] W. A. Groen, F. P. F. Van Berkel, D. J. W. Idjo, *Acta Crystallogr., Sect. C* **1986**, *42*, 1472.
[16] H. C. Van Duivenboden, D. J. W. Idjo, *Acta Crystallogr., Sect. C* **1986**, *42*, 52.
[17] J. A. Alonso, M. T. Casais, M. J. Martínez-Lope, J. L. Martínez, P. Velasco, A. Muñoz, M. T. Fernández-Díaz, *Chem. Mater.* **2000**, *12*, 161.
[18] N. E. Brese, M. O'Keefe, *Acta Crystallogr., Sect. B* **1991**, *47*, 192.
[19] J. Rodriguez-Carvajal, *Phys. B (Amsterdam)* **1993**, *192*, 55

Received: September 29, 2008
Published Online: February 3, 2009

